IMA Journal of Applied Mathematics (2005) 1−23
doi: 10.1093/imamat/hxh000

On the dynamics of a high speed coned fluid lubricated bearing

N. Y. BAILEY
University Technology Centre in Gas Turbine Transmission Systems, Faculty of Engineering, University of Nottingham, Nottingham, NG7 2RD, UK

K. A. CLIFFE, S. HIBBERD *
School of Mathematical Sciences, University of Nottingham, Nottingham, NG7 2RD, UK
* *Corresponding author:stephen.hibberd@nottingham.ac.uk*

AND

H. POWER
Fuels and Power Technology Research Division, Faculty of Engineering, University of Nottingham, Nottingham, NG7 2RD, UK

[Received on]

An incompressible air-flow model for a fluid film bearing is derived using a modified Reynolds equation for the thin-film dynamics of a rapidly rotating rotor and stator. Mathematical and numerical modelling is applied to the coupled processes of the fluid-flow through the bearing and the axial motion of the rotor and stator. This work focuses on extending previous studies to incorporate the dynamics of a coned rotor operating at high speeds and an incompressible lubrication approximation. The dynamics of fully coupled unsteady bearing motion and associated forcing of the rotor with axial periodic oscillations is studied. The axial motion of the stator is modelled as a spring-mass-damper system that responds to the rotor displacement through the film dynamics. In order to solve the modified Reynolds equation and stator equation simultaneously a new variable is introduced, namely the time dependent face clearance. This leads to explicit analytical expressions for the pressure and force in terms of the face clearance and the stator equation is transformed to a nonlinear second-order non-autonomous ordinary differential equation for the face clearance. Applying a transient solver gives solutions settling down to a stable periodic behaviour which motivates seeking a solver for periodic solutions. A Fourier spectral collocation scheme is derived to compute the periodic time dependent face clearance. Both solvers have matching periodic solutions of $O(1)$ with an absolute error of order of magnitude 10^{-5}. The dynamics of the unsteady bearing are examined for a range of pressure gradients and configurations including an asymptotic investigation of small face clearance associated with a start-up transient. Results are provided relating to changes in the width of bearing, strength of spring holding stator to its housing, damping of the stator and strength of the force coupling and rotor mass. The dynamics of the bearing are also investigated relative to values of key system parameters including the coning of the rotor, rotation speed and value of the bearing squeeze number. A parameter investigation is undertaken to highlight ideal bearing configurations to maximise load carrying capacity, fluid stiffness and damping.

Keywords: incompressible, Reynolds equation, periodic forcing, film clearance, bearing dynamics.

1 Introduction

Fluid lubricated bearing technology comprises two structural components of a rotor and a stator separated by a thin air-film, which experiences relative rotational motion. A thin air-film is employed to maintain a clearance between rotating and stationary elements when subjected to external axial loads

requiring a squeeze-film or hydrodynamic force generated by the dynamic motion of the bearing faces, enhancing the air-film pressure. Air-film lubrication is designed to provide improved performance for applications which are characterised by high differential speed operation which require low frictional losses. Gas bearings have the advantage of dispensing with leaky or contaminant-prone liquid lubricants, so can be cleaner in this sense. For industrial applications a comprehensive understanding of air-rotor-stator dynamics is vital since new technology requires bearings that can operate at higher rotational speeds, carry greater loads and maintain smaller clearances. Current applications of air-film bearings include hard disk drives, industrial generators and small gas turbine engines.

Thin film models often neglect inertia due to the 'classical lubrication' approximation, but this is not always accurate. Early work by Tuck & Bentwich (1983) studied lubrication with comparable viscous and inertia forces using a rigid plane thin sheet sliding steadily close to a plane wall. Wilson & Duffy (1998) extended the concept to fluid flow in a slender non-uniform cross sectional channel driven by relative motion of the boundary conditions in which viscous and inertia forces are comparable. The effect of inertia on air-flow in a hydrostatic seal of annular geometry was investigated by Brunetiére & Tournerie (2006). On the steady seal clearance the effect is small, with lowered air leakage, pressure across the seal face and rotor-stator clearance. Results are from comparison of the inertial model Brunetiére *et al.* (2003) and previous inertialess model Brunetiére *et al.* (2003).

Slider bearings employ a thin lubricating air-film to separate two non-parallel moving plates, with applications including read-write head in a computer hard disk drive which have negligible error tolerances, require low frictional losses while operating in a predictable manner at high speeds. Witelski (1998) studied the dynamics of the vertical motion of air bearing sliders presenting new results for the interaction of a compressible gas flow with a movable rigid surface. Linear stability analysis and perturbation methods were also undertaken. Further study was done by Witelski & Hendricks (2008) on the dynamics and stability of tapered air bearing sliders using analytical methods, and linear stability analysis yielded insight into the behaviour of the slider. Whereas Malvano *et al.* (1999) examined a lubricated slider bearing where the whole flow field is subdivided into three regions, since the elementary theory of lubrication does not allow to describe the pressure build up at the entrance section. A sliding externally pressurized gas bearing with parallel surfaces was theoretically investigated by Hasegawa & Izuchi (1982), taking inertia effects due to lubricant compressibility into account.

Lygren & Andersson (2000) studied turbulent flow between a rotating and stationary disk with direct numerical simulations performed obtaining steady state solutions, while McDarby & Smith (2007) modelled the fully turbulent flow induced on a rotating disk in unbounded fluid using a more analytical approach that previously seen. An experimental study on turbulent flow due to an enclosed rotation disk was undertaken by Itoh *et al.* (1991) for velocity distributions and Reynolds stress.

Green & Etison (1983) identified that the air film is a major component of the bearing so its dynamic properties must be understood if a full analysis of the bearing is to be performed. The concept of a squeeze film bearing, which has two coaxial discs separated by a thin air film, was first introduced by Salbu (1964) who considered bearings operating in highly vibrational environments and undergoing significant disturbances in the axial direction. Malanoski & Waldron (1973) examined a bearing with the rotor and stator being annuli rather than disks that had air-flow driven by a pressure gradient. They considered the feasibility of employing fluid lubricated technology for aero-engine use, discovering that the air-film thickness decreased when the force applied increased for a range of operating speeds. More recently fluid lubricated bearings have been of great interest in specialist turbomachinery applications with investigations continuing in many areas, such as those considered by San Andrés & Chirathadam (2011) and San Andrés & Kim (2008).

Fluid lubricated bearings have characteristic advantages over oil bearings, especially if their design

can provide sufficiently stiff and responsive fluid lubricated capabilities to make use of local dynamic effects to maintain a sufficient gap between the rotating and stationary elements. However too small a film thickness increases friction losses resulting in excessive wear and could lead to catastrophic collisions between the faces from induced vibrations, particularly at high rotation rates. Thus an appropriate air film gap must be maintained at all times in order to ensure safe and reliable operation as shown by Etison (1982). Designs of fluid lubricated technology commonly consist of a non-uniform rotor surface, with high differential pressures generating a hydrodynamic lifting force on the stator. Separation of the rotor and stator is maintained, improving the load carrying capacity of the bearing. Lift generating features on the rotor maybe employed in a number of designs, for example a spiral groove on the rotor as given by Zirkelback & San Andrés (1999) or foil sectors on the bearing surface, presented by Agrawal (1997). Sayma *et al.* (2002) demonstrated reliance on a high-shaft speed to maintain a sufficient force. Demand for new technologies with increased efficiency has lead to investigation of these and additional novel bearing designs.

Coned bearings have non-parallel faces caused by the deflection of the rotor or stator. Green (1987) showed coning may occur inadvertently due to manufacturing imperfections or misalignment with respect to the axis of rotation or purposefully to generate lift within the bearing and increase its load carrying capacity. Coning is well documented and can be a recurrent problem but its dynamical behaviour is not fully understood. Further the degree of complexity and difficulty of obtaining results limit the experimental analysis of the problem.

A mathematical formulation of the Reynolds equation for high speed motion of parallel rotor and stator is given by Garratt *et al.* (2010), (2011). The effects of compressibility in a fluid lubricated bearing can be neglected when possible oscillations have a low frequency and the Mach number is less than about 0.3, e.g. see pp 167-171, Batchelor (1967). An incompressible air flow model in an oil bearing has been reported to match well with experimental results in some cases but limitations were highlighted by Parkins & Stanley (1982), suggesting that when using lubrication theory retaining the effects of inertia could increase the predictive capacity of the model.

The purpose of this paper is to develop a mathematical model for high speed smooth coned rotor operation incorporating air-rotor-stator dynamics for a fully coupled unsteady bearing. Appropriate modelling, analytical and numerical analysis is carried out to identify the main operating characteristics of fluid lubricated technology and a parameter study is carried out to identify possible destabilising behaviour.

A mathematical model for incompressible flow in a high speed coaxial face bearing configuration is derived in section 2. This follows the approach adopted by Garratt *et al.* (2010) for compressible flow in a parallel plate bearing, leading to a modified Reynolds equation incorporating coning of the rotor and leading order inertia effects due to rotation. Axial motion of the stator is modelled as a spring-mass-damper system and analysis of periodic oscillations used to simulate possible destabilising behaviour of extreme operating systems. Section 3 gives the formulation for the fully coupled unsteady model which is simplified by introducing the time dependent face clearance as a new variable, thus enabling the pressure and force to be solved analytically. The modified stator equation is then transformed to a nonlinear second-order non-autonomous ordinary differential equation with respect to the time dependent face clearance coupled via the force. Solving numerically using a transient solver leads to an investigation of stable periodic solutions, these periodic solutions are explored using a Fourier spectral collocation numerical scheme. A small gap asymptotic analysis is provided to investigate if face contact can occur from an initial start-up transient. Results in section 5 show that if the rotor is disturbed then the bearing would remain stable enough to function for oscillations with amplitude $\varepsilon \leqslant 0.8$. The behaviour of an unsteady bearing is examined for a range of parameters corresponding to changes in structural and cou-

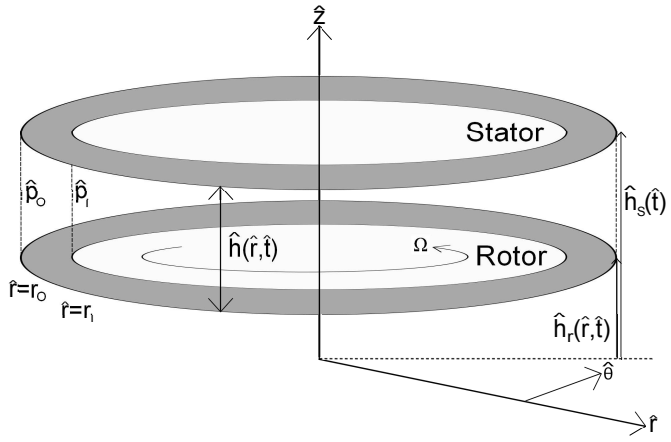

FIG. 2.1: Geometry of a fluid lubricated bearing in an axisymmetric dimensional cylindrical polar coordinate system $(\hat{\mathbf{r}}, \hat{\theta}, \hat{\mathbf{z}})$.

pling characteristics. The dynamics of the bearing is also investigated relative to values of key system parameters: the width of bearing, pressurisation, coning angle, rotation speed and value of the bearing squeeze number. This paper contains some complex and extended algebraic manipulation which has been checked using computer algebraic systems (Matlab symbolic package and Mathematica).

2 Mathematical model formulation for a high-speed coned bearing

A simplified mathematical model is developed by retaining the key features of the fluid lubricated bearing shown in Figure 2.1 for a parallel rotor/stator configuration. The rotor and the stator are modelled as a pair of coaxial annuli with inner and outer dimensional radii of r_I and r_O, respectively, and rotor angular rotation $\hat{\Omega}$. Pressures $\hat{p}_I$ and $\hat{p}_O$ are imposed at the inner and outer radii of the bearing respectively, allowing a pressure gradient to be imposed to drive a radial flow. The axisymmetric rotor-stator clearance is given in dimensional variables by

$$\hat{h}(\hat{r},\hat{t}) = \hat{h}_s(\hat{t}) - \hat{h}_r(\hat{r},\hat{t}), \tag{2.1}$$

where $\hat{h}_s$ and $\hat{h}_r$ are the stator and rotor heights, respectively.

A bearing model is considered where the rotor has a fixed coning angle $\hat{\beta}$, assumed to be small $\hat{\beta} \ll 1$, as shown in Figure 2.2 and $\hat{h}_r(\hat{r},\hat{t})$ is the reference height of the rotor. A positive coning angle $\hat{\beta} > 0$ is associated with a diverging channel flow for an internally pressurised bearing and for negative coning angles $\hat{\beta} < 0$, a converging channel. The rotor is assumed to be forced by an externally prescribed axial oscillation of frequency $\hat{f}$, amplitude εh_0, where h_0 is the dimensional film thickness at the inner radius, and angular frequency $\hat{\omega} = 2\pi\hat{f}$. The position of the rotor is given by

$$\hat{h}_r(\hat{r},\hat{t}) = \varepsilon h_0 \sin(\hat{\omega}\hat{t}) - (\hat{r} - r_I)\tan\hat{\beta}. \tag{2.2}$$

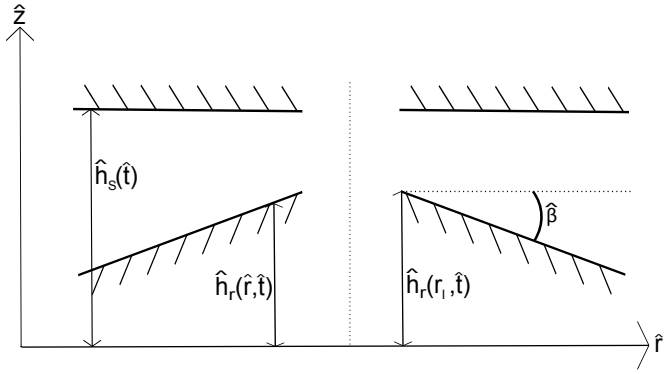

FIG. 2.2: Cross sectional view of a bearing with a positive angle of coning.

A model for the incompressible air-flow through the bearing may be derived from the Navier-Stokes momentum and continuity equations

$$\hat{\rho}\left(\frac{\partial \hat{\mathbf{u}}}{\partial \hat{t}} + (\hat{\mathbf{u}}\cdot\hat{\nabla})\hat{\mathbf{u}}\right) = -\hat{\nabla}\hat{p} + \mu\hat{\nabla}^2\hat{\mathbf{u}} + \mathbf{b}, \qquad \hat{\nabla}\cdot\ \hat{\mathbf{u}} = 0, \tag{2.3}$$

where ρ is the density, μ the dynamic viscosity and $\mathbf{b}$ represents external body forces such as gravity.

It is assumed that the bearing configuration is axisymmetric and the velocity field is $\hat{\mathbf{u}} = (\hat{u}, \hat{v}, \hat{w})$ in cylindrical polar coordinates.

Since both the stator and rotor are solid surfaces, no normal flow and a no-slip boundary condition must be imposed on both of these surfaces. The stator velocity boundary conditions are

$$\hat{u} = 0, \quad \hat{v} = 0, \quad \hat{w} = \frac{\mathrm{d}\hat{h}_s}{\mathrm{d}\hat{t}} \quad \text{at} \quad \hat{z} = \hat{h}_s. \tag{2.4}$$

For the coned rotor a new set of cylindrical polar axes is defined on the face of the rotor as $(\hat{\mathbf{e}}^r_{\mathbf{r}}, \hat{\mathbf{e}}^r_{\theta}, \hat{\mathbf{e}}^r_{\mathbf{z}})$ with $\hat{\mathbf{e}}^r_{\mathbf{r}}$ tangential and $\hat{\mathbf{e}}^r_{\mathbf{z}}$ normal to the face of the rotor. This enables the no-slip condition on the rotor to be expressed in the primary coordinate system in which the Navier Stokes equations are solved. The new coordinate system along with the primary coordinate system $(\hat{\mathbf{e}}_{\mathbf{r}}, \hat{\mathbf{e}}_{\theta}, \hat{\mathbf{e}}_{\mathbf{z}})$ are shown in Figure 2.3. The air velocity in the primary coordinate system and the coordinate system on the face of the rotor is

$$\hat{\mathbf{u}} = \begin{pmatrix} \hat{u} \\ \hat{v} \\ \hat{w} \end{pmatrix} \quad \text{and} \quad \hat{\mathbf{u}}^{\mathbf{r}} = \begin{pmatrix} \hat{u}\cos\hat{\beta} - \hat{w}\sin\hat{\beta} \\ \hat{v} \\ \hat{u}\sin\hat{\beta} + \hat{w}\cos\hat{\beta} \end{pmatrix}, \tag{2.5}$$

respectively, and the tangential flow on the face of the rotor is

$$\hat{\mathbf{u}}^r - \left(\hat{\mathbf{u}}^r\cdot\hat{\mathbf{e}}^r_z\right)\hat{\mathbf{e}}^r_z = \begin{pmatrix} \hat{u}\cos\hat{\beta} - \hat{w}\sin\hat{\beta} \\ \hat{v} \\ 0 \end{pmatrix}, \tag{2.6}$$

where $\hat{\mathbf{e}}^r_z$ is the normal to the coned rotor.

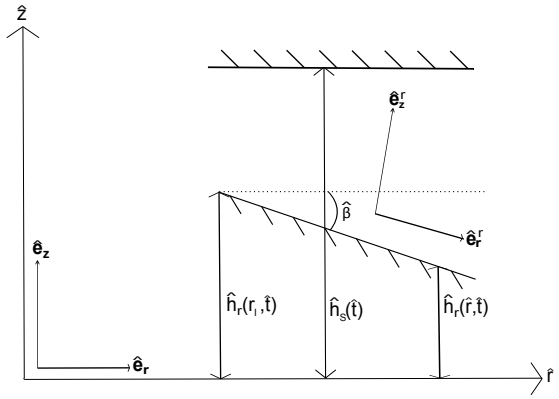

FIG. 2.3: Configuration of the $(\hat{r},\hat{z})$ plane with cylindrical polar coordinate systems; primary $(\hat{\mathbf{e}}_\mathbf{r},\hat{\mathbf{e}}_\theta,\hat{\mathbf{e}}_\mathbf{z})$ and vectors on face of rotor $(\hat{\mathbf{e}}^r_\mathbf{r},\hat{\mathbf{e}}^r_\theta,\hat{\mathbf{e}}^r_\mathbf{z})$.

The no-slip condition on the rotor requires that the fluid velocity is equal to the rotor velocity which has zero radial and axial velocity but azimuthal velocity of magnitude $\Omega(\hat{t})\hat{r}$ giving the conditions

$$\hat{u} = \tan\hat{\beta}\ \hat{w} \quad \text{and} \quad \hat{v} = \Omega(\hat{t})\hat{r} \quad \text{at} \quad \hat{z} = \hat{h}_r, \tag{2.7a}$$

and the kinematic condition on the rotor gives

$$\hat{w} = \cos^2\hat{\beta}\,\frac{\partial \hat{h}_r}{\partial \hat{t}}. \tag{2.7b}$$

To identify the primary physical processes at leading order the Navier-Stokes equations are expressed using a set of dimensionless variables. A typical pressure value of P gives the dimensionless variable $p = \hat{p}/P$ and for a typical time scale $T = 1/\hat{\omega}$ the dimensionless time variable $t = \hat{t}/T$. The radius of the bearing r_0 and the equilibrium height difference between the rotor and stator h_0 giving the radial variable $r = \hat{r}/r_0$ and axial variable $z = \hat{z}/h_0$. The non-dimensional air velocity components are given by $u = \hat{u}/U$, $v = \hat{v}/V$ and $w = \hat{w}/W$ for typical radial, azimuthal and axial velocities U, V and W respectively. Since the rotor rotates at $\hat{\Omega}$ then $V = \Omega r_0$ whereas the axial velocity $W = h_0/T$ due to the velocity boundary conditions (2.7).

These can be readily applied to the Navier-Stokes momentum and continuity equations (A.1) with the radial and azimuthal Reynolds numbers and the Reynolds number ratio given, respectively, as

$$Re_U = \frac{\hat{\rho} r_0 U}{\mu}, \quad Re_\Omega = \frac{\hat{\rho} r_0^2 \hat{\Omega}}{\mu} \quad \text{and} \quad Re^* = \frac{Re_\Omega}{Re_U} = \frac{\hat{\Omega} r_0}{U}. \tag{2.8}$$

The aspect ratio δ_0, squeeze number $\hat{\sigma}$ and Froude number Fr are defined as

$$\delta_0 = \frac{h_0}{r_0}, \quad \hat{\sigma} = \frac{r_0}{UT} \quad \text{and} \quad Fr = \frac{U}{\sqrt{g h_0}}, \tag{2.9}$$

respectively, where g is the acceleration due to gravity. For more practical cases $\delta_0 \ll 1$, justifying the use of the lubrication approximation. The squeeze number $\hat{\sigma}$ characterises any time dependent effects

whilst the Froude number Fr parametrises the importance of the gravitational effects relative to the radial flow. To ensure that the effects of viscosity are retained at leading order the pressure is scaled as $P = \mu r_R U/h_0^2$. Classical lubrication theory allows all inertia to be neglected due to the reduced Reynolds number being small, $Re_U \delta_0^2 \ll 1$. However, in the case of high-speed bearing operation the ratio of the Reynolds numbers Re^* is not always negligible and an additional term must be considered, see Garratt *et al.* (2010). Since $\delta_0 \ll 1$ it is assumed that gravity can be neglected, (since $Re_U \delta_0^2 Fr^{-2} \ll 1$). This condition is satisfied if the typical radial velocity U is such that the Froude number is $O(1)$.

To leading order the Navier-Stokes momentum equations become

$$-\eta \frac{v^2}{r} = -\frac{\partial p}{\partial r} + \frac{\partial^2 u}{\partial z^2}, \tag{2.10}$$

$$0 = \frac{\partial^2 v}{\partial z^2}, \tag{2.11}$$

$$0 = \frac{\partial p}{\partial z}, \tag{2.12}$$

where the speed parameter $\eta = Re_U \delta_0^2 (Re^*)^2$ represents the effect of inertia due to rotation. The axial momentum equation implies that the pressure is independent of z. Similarly the continuity equation becomes

$$\frac{1}{r}\frac{\partial}{\partial r}(ru) + \hat{\sigma}\frac{\partial w}{\partial z} = 0. \tag{2.13}$$

Derivation of the leading order Navier-Stokes momentum and continuity equations are given in Appendix A, following the approach in Garratt *et al.* (2010, 2011).

The periodically forced rotor position becomes

$$h_r(r,t) = \varepsilon \sin t - (r-a)\beta, \tag{2.14}$$

where $a = r_I/r_0$ is a measure of the bearing width ($0 < a < 1$) and $\beta = \tan\hat{\beta}/\delta_0$. The scaling on the coning angle comes from the lubrication approximation in which the aspect ratio δ_0 is small and the rates of strain and stress are very large due to viscosity in the fluid layer provided there is a dominant direction of flow. The large stress causes a large pressure to develop when using a suitable configuration of bearing, in which the coning angle $\hat{\beta}$ is of equivalent size of the aspect ratio $\delta_0 \ll 1$ Batchelor (1967) (pg 219). Thus β must have at most $O(1)$ to make lubrication theory hold.

The boundary conditions on the face of the rotor and stator become to leading order

$$u = 0, \quad v = r, \quad w = \frac{\partial h_r}{\partial t} \quad \text{at} \quad z = h_r(r,t), \tag{2.15}$$

$$u = 0, \quad v = 0, \quad w = \frac{\mathrm{d}h_s}{\mathrm{d}t} \quad \text{at} \quad z = h_s(t). \tag{2.16}$$

Applying the above gives the radial, azimuthal and axial velocities, respectively, as

$$\begin{aligned} u(r,z,t) &= \frac{1}{2}\frac{\partial p}{\partial r}(z-h_s)(z-h_r) \\ &\quad -\frac{\eta r}{12h^2}(z-h_s)(z-h_r)\left(z^2+(h_r-3h_s)z+3h_s^2-3h_rh_s+h_r^2\right), \\ v(r,z,t) &= \frac{r}{h}(h_s-z), \\ w(r,z,t) &= \frac{\partial h_r}{\partial t}-\frac{1}{\sigma r}\frac{\partial}{\partial r}\left(r(z-h_r)^2(2z+h_r-3h_s)\frac{\partial p}{\partial r}\right) \\ &\quad -\frac{\lambda}{3\sigma r}\frac{\partial}{\partial r}\left(\frac{r^2}{h^2}(z-h_r)^2\left(2(z-h_r)^3-10(z-h_r)^2h+20(z-h_r)h^2-15h^3\right)\right) \end{aligned} \tag{2.17}$$

where parameter $\lambda = 3/10\eta$ and $\sigma = 12\hat{\sigma}$.

Integrating the continuity equation between the rotor and stator, and applying the Leibniz integral rule and the kinematic boundary conditions gives the modified unsteady Reynolds equation

$$\sigma\frac{\partial h}{\partial t}-\frac{1}{r}\frac{\partial}{\partial r}\left(rh^3\frac{\partial p}{\partial r}\right)+\frac{\lambda}{r}\frac{\partial}{\partial r}\left(r^2h^3\right)=0. \tag{2.18}$$

This modified Reynolds equation expresses the relationship between the pressure $p(r,t)$ and the film thickness $h(r,t)$. If $\lambda \ll 1$ then the centrifugal effects are negligible and we recover the classic Reynolds equation.

In dimensionless variables the pressures at the inner and outer radii of the bearing are

$$p = p_I \text{ at } r = a, \text{ and } p = p_O \text{ at } r = 1. \tag{2.19}$$

In dimensionless variables the rotor-stator clearance is

$$h(r,t) = h_s(t) - \varepsilon\sin t + (r-a)\beta, \tag{2.20}$$

when the rotor has periodically oscillating forcing $h_r(t) = \varepsilon\sin t$, where ε is the non dimensional amplitude of forced rotor oscillations.

The axial displacement of the stator is modelled using Newton's second law as a spring-mass-damper system giving the axial position of the stator in dimensionless variables as

$$\frac{\mathrm{d}^2h_s}{\mathrm{d}t^2}+D_a\frac{\mathrm{d}h_s}{\mathrm{d}t}+K_z(h_s-1)=\alpha F(t). \tag{2.21}$$

Taking the mass of the stator as m, F is the resultant dimensionless axial force on the stator

$$F(t) = 2\pi\int_a^1 (p-p_a)r\mathrm{d}r, \tag{2.22}$$

where p_a is the atmospheric pressure. $D_a = \hat{D}_a/m\hat{\omega}$ and $K_z = \hat{K}_z/m\hat{\omega}^2$ are the dimensionless damping and spring parameters respectively, where $\hat{D}_a$ and $\hat{K}_z$ are the dimensional linear damping and stiffness coefficients, respectively, that are applied to constrain the stator displacement relative to its equilibrium position $h_s(a,t)$. The strength of the force coupling is characterized by $\alpha = \mu U/m\hat{\omega}^2\delta_0^3$.

3 Derivation of face clearance equation

In the coupled bearing the displacement of the stator, h_s, due to the periodic forcing of the rotor and the air-film dynamics satisfies the coupled second-order integro-differential equation, (2.21).

It is mathematically convenient to introduce the time dependent magnitude of the bearing gap as

$$g(t) = h_s(t) - h_r(a,t), \tag{3.1}$$

which is referred to as the face clearance. The rotor-stator film thickness, $h(r,t)$, then becomes

$$h(r,t) = g(t) + (r-a)\beta, \tag{3.2}$$

valid in the region $a \leqslant r \leqslant 1$. This allows a single equation to be derived dependent upon $g(t)$ which characterises the whole system and the r dependence is removed.

Substituting $g(t)$ into the modified Reynolds equation (2.18), integrating twice and imposing the pressure boundary conditions (2.19), gives after some algebra, the pressure in the air-film as

$$p = p_I + \frac{\lambda}{2}(r^2-a^2) + \left(p_O - p_I - \frac{\lambda}{2}(1-a^2)\right)\frac{G(r)}{G(1)} + \frac{\sigma}{2}\left(H(r) - \frac{H(1)}{G(1)}G(r)\right)\frac{\mathrm{d}g}{\mathrm{d}t}. \tag{3.3}$$

The integrals $G(r)$ and $H(r)$ are calculated analytically and are given below. The simplest case of parallel plates $\beta = 0$ is denoted with subscript 0 and calculated using a modified method to avoid dividing through by a zero factor. In (3.3)

$$\begin{aligned} G(r) &= \int_a^r \frac{\mathrm{d}r}{r(g+\beta\,(r-a))^3} \\ &= \frac{1}{(g-a\beta)^3}\ln\left(\frac{gr}{a(g+(r-a)\beta)}\right) \\ &\quad + \frac{1}{2(g-a\beta)^2}\left(\frac{3g+(2r-3a)\beta}{(g+(r-a)\beta)^2} - \frac{3g-a\beta}{g^2}\right), \end{aligned} \tag{3.4a}$$

$$G_0(r) = \int_a^r \frac{\mathrm{d}r}{rg^3} = \frac{1}{g^3}(\ln r - \ln a), \tag{3.4b}$$

and

$$\begin{aligned} H(r) &= \int_a^r \frac{r\,\mathrm{d}r}{(g+(r-a)\beta)^3} \\ &= \frac{1}{\beta^2}\left(-\frac{1}{g+(r-a)\beta} + \frac{g-a\beta}{2(g+(r-a)\beta)^2} + \frac{g+a\beta}{2g^2}\right), \end{aligned} \tag{3.5a}$$

$$H_0(r) = \int_a^r \frac{r\,\mathrm{d}r}{g^3} = \frac{1}{g^3}\left(\frac{r^2-a^2}{2}\right). \tag{3.5b}$$

The force on the stator is evaluated from equation (2.22) using the pressure expression in equation (3.3) giving

$$\begin{aligned} F(t) &= \pi\left(p_I(1-a^2) + \frac{\lambda}{4}(1-a^2)^2 + 2\left(p_O - p_I - \frac{\lambda}{2}(1-a^2)\right)\frac{G_I}{G(1)}\right. \\ &\quad \left. + \sigma\left(H_I - \frac{H(1)}{G(1)}G_I\right)\frac{\mathrm{d}g}{\mathrm{d}t} - p_a(1-a^2)\right). \end{aligned} \tag{3.6}$$

The integrals $G(1)$ and $H(1)$ can be found from equations (3.4) and (3.5) respectively, G_I and H_I are given as

$$\begin{aligned} G_I &= \int_a^1 rG(r)\mathrm{d}r \\ &= \frac{1}{2(g-a\beta)^3}\ln\left(\frac{g}{a(g+(1-a)\beta)}\right) \\ &\quad + \frac{1}{2(g-a\beta)^2}\left(\frac{(1-a)}{\beta} - \frac{(1-a^2)(3g-a\beta)}{2g^2}\right) \\ &\quad + \frac{1}{2\beta^2}\left(\frac{1}{g+(1-a)\beta} - \frac{1}{g}\right), \end{aligned} \tag{3.7a}$$

$$G_{0I} = \int_a^1 rG_0(r)\mathrm{d}r = \frac{1}{g^3}\left(\frac{a^2-1}{4} - \frac{1}{2}\ln a\right), \tag{3.7b}$$

and

$$\begin{aligned} H_I &= \int_a^1 rH(r)\mathrm{d}r \\ &= \frac{1}{\beta^2}\left(\frac{a-1}{\beta} + \frac{(1-a^2)(g+a\beta)}{4g^2} + \frac{3(g-a\beta)}{2\beta^2}\ln\left(\frac{g+(1-a)\beta}{g}\right)\right. \\ &\quad \left. + \frac{(g-a\beta)^2}{2\beta^2}\left(\frac{1}{(g+(1-a)\beta)} - \frac{1}{g}\right)\right), \end{aligned} \tag{3.8a}$$

$$H_{0I} = \int_a^1 rH_0(r)\mathrm{d}r = \frac{1}{8g^3}(1-a^2)^2. \tag{3.8b}$$

Rewriting (3.6) in terms of gap expressions $A(g)$ and $B(g)$ gives

$$F(t) = \pi\left(A(g) + B(g)\frac{\mathrm{d}g}{\mathrm{d}t}\right), \tag{3.9}$$

where

$$A(g) = p_I(1-a^2) + \frac{\lambda}{4}(1-a^2)^2 - p_a(1-a^2) + 2\left(p_O - p_I - \frac{\lambda}{2}(1-a^2)\right)\frac{G_I}{G(1)}, \tag{3.10}$$

and

$$B(g) = \sigma\left(H_I - \frac{H(1)}{G(1)}G_I\right). \tag{3.11}$$

Substituting the force expression (3.9) and stator height (3.2) into the governing stator equation (2.21) results in the nonlinear, second-order, non-autonomous ordinary differential equation

$$\frac{\mathrm{d}^2g}{\mathrm{d}t^2} + (D_a - \alpha\pi B(g))\frac{\mathrm{d}g}{\mathrm{d}t} + K_z(g-1) - \alpha\pi A(g) = \varepsilon((1-K_z)\sin t - D_a\cos t), \tag{3.12}$$

for the time dependent face clearance in the air-film.

The modified stator equation (3.12) can be written in a general form

$$\frac{\mathrm{d}^2 g}{\mathrm{d}t^2} + D(g)\frac{\mathrm{d}g}{\mathrm{d}t} + S(g) = \Upsilon \sin(t+\phi), \tag{3.13}$$

where

$$D(g) = D_a - \alpha\pi B(g),\ S(g) = K_z(g-1) - \alpha\pi A(g),\ \Upsilon\sin(t+\phi) = \varepsilon((1-K_z)\sin t - D_a\cos t), \tag{3.14}$$

with $\tan(\phi) = D_a/(K_z-1)$. The differential equation (3.13) corresponds to a harmonically forced oscillator equation with nonlinear damping coefficient $D(g)$, nonlinear represented stiffness $S(g)$ and temporal forcing of the system $\Upsilon\sin(t+\phi)$ from a driven oscillator. Thus the governing coupled, second order, integro-differential equation has been transformed to a nonlinear, second order, non-autonomous ordinary differential equation which can be solved more readily.

The total stiffness of the system K_{zT} is found by differentiating $S(g)$ with respect to the time dependent face clearance $g(t)$;

$$K_{zT} = \frac{\mathrm{d}S}{\mathrm{d}g} = K_z - \alpha\pi\frac{\mathrm{d}A(g)}{\mathrm{d}g}, \tag{3.15}$$

where K_z is the contribution from the structure and $-\alpha\pi\mathrm{d}A(g)/\mathrm{d}g$ is the fluid stiffness, K_{Zf}. From the definition (3.10) of $A(g)$ have

$$\frac{\mathrm{d}A}{\mathrm{d}g} = (2(P_O - P_I) - \lambda(1-a^2))\left(\frac{\partial G_I}{\partial g}\frac{1}{G(1)} - \frac{G_I}{G(1)^2}\frac{\partial G(1)}{\partial g}\right). \tag{3.16}$$

In (3.16) $G(1)$ and G_I can be found from (3.4) and (3.7), respectively, and

$$\begin{aligned}
\frac{\partial G(r)}{\partial g} &= \frac{3}{(g-a\beta)^4}\ln\left(\frac{a(g+(r-a)\beta)}{gr}\right) + \frac{3}{(g-a\beta)^3}\left(\frac{1}{g} - \frac{1}{g+(r-a)\beta}\right) \\
&\quad + \frac{3}{2(g-a\beta)^2}\left(\frac{1}{g^2} - \frac{1}{(g+(r-a)\beta)^2}\right) \\
&\quad + \frac{1}{g-a\beta}\left(\frac{1}{g^3} - \frac{1}{(g+(r-a)\beta)^3}\right), \qquad (3.17a) \\
\frac{\partial G_0(r)}{\partial g} &= -\frac{3}{g^4}(\ln r - \ln a), \qquad (3.17b)
\end{aligned}$$

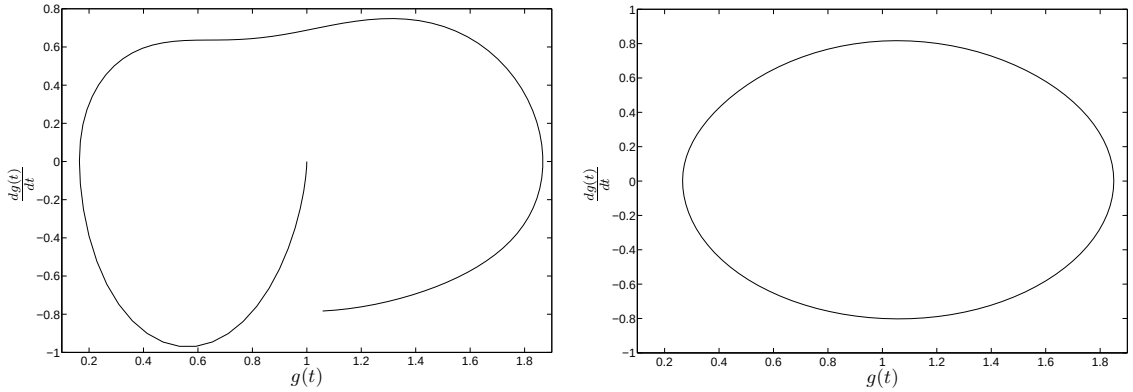

(a) (b)

FIG. 3.1: Face clearance plotted against its time derivative for an unsteady narrow internally pressurised bearing a) first time period and b) tenth time period; $a = 0.8$, $\beta = -0.3$, $\varepsilon = 0.8$, $\lambda = 1$, $\sigma = 1$, $\alpha = 1$, $K_z = 10$ and $D_a = 1$.

and

$$\begin{aligned}\frac{\partial G_I}{\partial g} &= \frac{1}{(g-a\beta)^4}\left(\frac{3}{2}\ln\left(\frac{a(g+(1-a)\beta)}{g}\right)+\frac{9}{4}+\frac{3a}{2}+\frac{3a^2}{4}+\frac{3a\beta}{g}\left(\frac{a^2}{2}-1\right)\right.\\ &\quad+\frac{3a^2\beta^2}{4g^2}(1-a^2)-\frac{3g}{\beta}\left(a-\frac{1}{2}\right)+\frac{3g^2}{2\beta^2}\\ &\quad\left.+\frac{1}{2(g+(1-a)\beta)}\left(3a^3\beta-9ga^2+\frac{9g^2a}{\beta}-\frac{3g^3}{\beta^2}\right)\right)\\ &\quad+\frac{1}{(g-a\beta)^3}\left(\frac{1}{2g}+\frac{a\beta}{g^2}\left(\frac{a^2}{2}-1\right)+\frac{a^2\beta^2}{2g^3}(1-a^2)+\frac{1}{\beta}\left(\frac{1}{2}+a\right)-\frac{g}{\beta^2}\right.\\ &\quad+\frac{1}{(g+(1-a)\beta)}\left(\frac{3a^2}{2}-\frac{1}{2}-\frac{3ag}{\beta}+\frac{3g^2}{2\beta^2}\right)\\ &\quad\left.+\frac{1}{2}(g+(1-a)\beta)^2\left(a^3\beta-3ga^2+\frac{3g^2a}{\beta}-\frac{g^3}{2\beta^2}\right)\right), \qquad (3.18a)\\ \frac{\partial G_{0I}}{\partial g} &= -\frac{3}{4g^4}\left((a^2-1)-2\ln a\right). \qquad (3.18b)\end{aligned}$$

The modified stator equation (3.13) was solved for the face clearance $g(t)$ in `Matlab` via a transient numerical ordinary differential stiff solver `ode45`.

Since the rotor motion is started impulsively, the transient solver runs until a stable periodic orbit is reached. Figure 3.1 shows the face clearance plotted against its time derivative for an unsteady narrow internally pressurised bearing for the first and tenth time period. The first cycle is incomplete implying the solution is transient, however by the tenth time period a closed orbit is achieved thus the solution converges to a stable periodic solution. The maximum absolute error of the solution, is calculated to be

of order 10^{-8}.

For periodic solutions a more direct and efficient numerical solver is used. A Fourier spectral collocation solver is introduced in which time derivatives in the modified stator equation (3.13) are given by spectral differentiation matrices leading to an algebraic equation problem. This is then solved for the time dependent face clearance via the Newton-Raphson method as given by Wolfram MathWorld (2011).

Implementing the spectral collocation scheme constructs the time dependent face clearance $g(t)$ using trigonometric polynomials at uniformly distributed time collocation points. The Fourier transform is used to derive the spectral differentiation matrices for evaluating the time derivative to give an algebraic equation

$$\xi(\mathbf{g}) \equiv \mathbf{D^2 g} + D(\mathbf{g})\mathbf{D^1 g} + \mathbf{S}(\mathbf{g}) - \Upsilon(t) = \mathbf{0}. \tag{3.19}$$

Here $\mathbf{g}$ is a vector of the face clearance calculated at the collocation points and $\mathbf{D^1}$ and $\mathbf{D^2}$ are spectral differentiation matrices found using Trefethen (2000) which express the first and second time derivatives at each collocation point, respectively. The initial guess is given as $g_0(t) = 1 - 0.8\sin t$.

Equation (3.19) is solved using the Newton-Raphson method

$$\mathbf{g}_{n+1} = \mathbf{g}_n - \left(\frac{\partial \xi}{\partial \mathbf{g}_n}\right)^{-1} \xi(\mathbf{g}_n), \quad \text{where} \quad \frac{\partial \xi}{\partial \mathbf{g}} = \mathbf{D^2} + D(\mathbf{g})\mathbf{D^1} + \frac{\partial D(\mathbf{g})}{\partial \mathbf{g}}\mathbf{D^1 g} + \frac{\partial S(\mathbf{g})}{\partial \mathbf{g}}. \tag{3.20}$$

$dS(\mathbf{g})/dg$ is the stiffness of the system given in (3.15) while $D(\mathbf{g})$ is expressed in (3.14) giving

$$\frac{\partial D(\mathbf{g})}{\partial \mathbf{g}} = -\alpha\pi \frac{\partial B(\mathbf{g})}{\partial \mathbf{g}}. \tag{3.21}$$

Equation (3.11) expresses the function $B(g)$ resulting in

$$\frac{\partial B(\mathbf{g})}{\partial \mathbf{g}} = \sigma\left(\frac{dH_I}{\partial \mathbf{g}} - \frac{G_I}{G(1)}\frac{\partial H(1)}{\partial \mathbf{g}} - \frac{H(1)}{G(1)}\frac{\partial G_I}{\partial \mathbf{g}} + \frac{H(1)}{G(1)^2}G_I\frac{\partial G(1)}{\partial \mathbf{g}}\right). \tag{3.22}$$

$G(1)$, $H(1)$ and G_I can be found from equations (3.4), (3.5) and (3.7) for coned and parallel face bearings, respectively, with

$$\begin{aligned}
\frac{\partial H(r)}{\partial g} &= \frac{1}{\beta^2}\left(\frac{3}{2}\left(\frac{1}{(g+(r-a)\beta)^2} - \frac{1}{g^2}\right)\right. \\
&\quad \left. +(g-a\beta)\left(\frac{1}{g^3} - \frac{1}{(g+(r-a)\beta)^3}\right)\right), \qquad (3.23a)\\
\frac{\partial H_0(r)}{\partial g} &= -\frac{3}{g^4}\frac{r^2-a^2}{2}, \qquad (3.23b)
\end{aligned}$$

and

$$\begin{aligned}
\frac{\partial H_I}{\partial g} &= \frac{1}{\beta^4}\left(-2 + \frac{3}{2}\ln\left(\frac{g+(1-a)\beta}{g}\right) + \frac{5g}{2(g+(1-a)\beta)} - \frac{g^2}{2(g+(1-a)\beta)^2}\right) \\
&\quad + \frac{1}{\beta^3}\left(\frac{3a}{2g} - \frac{5a}{2(g+(1-a)\beta)} + \frac{ga}{(g+(1-a)\beta)^2}\right) \\
&\quad + \frac{1}{\beta^2}\left(\frac{3a^2-1}{4g^2} - \frac{a^2}{2(g(1+(1-a)\beta)^2}\right) + \left(\frac{a}{2g^3\beta}(a^2-1)\right), \\
\frac{\partial H_{0I}}{\partial g} &= -\frac{3}{8g^4}(1-a^2)^2, \qquad (3.24a)
\end{aligned}$$

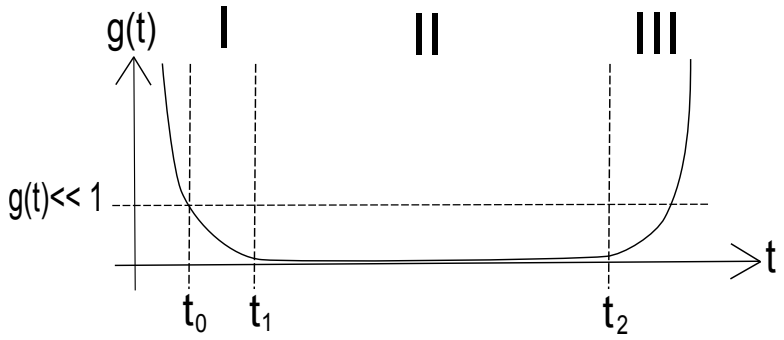

FIG. 4.1: Asymptotic regions for scaling of initial transient when $g \ll 1$.

The spectral collocation solver runs until the solution converges as defined by an error tolerance, tol, which is defined as

$$\| g_{n+1} - g_n \|_\infty < \text{tol}. \tag{3.25}$$

Both solvers give matching periodic solutions with an agreement to $O(10^{-5})$, with tol= $1\text{x}10^{-12}$ and Matlab solver tolerance of $2\text{x}10^{-12}$.

4 Small face clearance in limit $g(t) \ll 1$

A transient solution obtained numerically for rotor/stator position and face clearance $g(t)$ for large oscillations is given in Figure 5.2 and shows that within the first period the gap becomes very small for over approximately a third of a period. The numerical behaviour of the face clearance $g(t)$ in the limit $g \ll 1$ is examined asymptotically to investigate if face contact can occur. Parallel and coned bearings are examined separately.

Figure 4.1 shows three different regions for $g \ll 1$ suggested by Figure 5.2 where region I and region III are the transition to and from region II, respectively, where $g(t)$ is approximately a constant with minimum gap $g_{\min}$. If $g_{\min} > 0$ then face contact will not occur.

In the limit $g(t) \ll 1$ for a parallel bearing, equation (3.13) becomes to leading order

$$\frac{\mathrm{d}^2 g}{\mathrm{d}t^2} + \frac{\bar{B}}{g^3}\frac{\mathrm{d}g}{\mathrm{d}t} + K_z g - K = \Upsilon \sin(t+\phi), \tag{4.1}$$

with positive constants $\bar{B}$ and K given by

$$\bar{B} = -\alpha\pi\sigma\left(\frac{(1-a^2)^2}{8}\left(1+\frac{1}{\ln a}\right)+\frac{(1-a^2)}{4}\right), \quad K = -\alpha\pi A, \tag{4.2}$$

where A is given by equation (3.10) and of $O(1)$, also it is assumed $\Upsilon \gg 1$.

Solving equation (4.1) numerically subject to the same initial conditions as the full numerical equation (3.13) i.e. $g(0) = 1$ and $\mathrm{d}g/\mathrm{d}t(0) = 0$, shows a similar characteristic behaviour of the full numerical solution. Three asymptotic regions are identified as shown in Figure 4.1 with $| g(t) | \ll 1$, and approximate associated characteristic times t_0, t_1 and t_2. Region I has $\mathrm{d}g/\mathrm{d}t < 0$ and $| \mathrm{d}^2 g/\mathrm{d}t^2 | \gg 1$, region II has $\mathrm{d}g/\mathrm{d}t \ll 1$ and region III initiated by $\mathrm{d}g/\mathrm{d}t > 0$.

In region I, $|\,\mathrm{d}^2g/\mathrm{d}t^2\,| \gg 1$ so locally a short time behaviour is comparable to an inner boundary layer, where initial conditions become $g(t_0) = g_0$ and $\mathrm{d}g(t_0)/\mathrm{d}t = -\bar{\sigma}$, for given initial time t_0 and $\bar{\sigma} > 0$, say. Introducing $c = (1+2g_0^2\bar{\sigma})^{\frac{1}{2}}/g_0$, new inner time scale $\tau = \bar{B}c^3(t-t_0)$ and rescaling $y(\tau) = cg$, equation (4.1) becomes to leading order

$$\frac{\mathrm{d}^2y}{\mathrm{d}\tau^2} + \frac{1}{y^3}\frac{\mathrm{d}\,y}{\mathrm{d}\tau} = 0, \tag{4.3}$$

taking $y(0) = cg_0$ and $\mathrm{d}y(0)/\mathrm{d}\tau = -\bar{\sigma}/c^2$.

Solving subject to initial conditions, for narrowing face clearance gives an intrinsic algebraic relationship for $y = Y(\tau; g_0)$ as

$$\tanh^{-1}(y) - \tanh^{-1}(cg_0) + cg_0 - y = \frac{1}{2}\tau, \tag{4.4}$$

which is readily solved for y numerically by Newton's method.

Matching of the solution in region I to region II is when $\tau \to \infty$ with solution

$$y \to 1. \tag{4.5}$$

In region II a balance between the damping and forcing is assumed in (4.1) and so Υ is of $O(c^2)$ and new time scale $\bar{t} + t_0 = t$, where $\bar{t} = O(1)$, gives to leading order

$$\frac{\bar{B}}{g^3}\frac{\mathrm{d}g}{\mathrm{d}\bar{t}} - K = \Upsilon\sin(\bar{t} + \bar{\phi} + 2t_0), \tag{4.6}$$

where $\bar{\phi} + t_0 = \phi$. The solution is given as

$$g(\bar{t}) = \frac{\bar{B}^{\frac{1}{2}}}{\left(\bar{B}c^2 - 2K\bar{t} + 2\Upsilon(\cos(\bar{t}+\bar{\phi}+2t_0) - \cos(\bar{\phi}+2t_0))\right)^{\frac{1}{2}}}, \tag{4.7}$$

on matching the solution $g(\bar{t} = 0) = 1/c$ with region I.

Writing the solution in region I in terms of original variables gives,

$$g(t) = \frac{Y(\bar{B}c^3(t-t_0); g_0)}{c}, \tag{4.8}$$

and the composite solution in region I and II is

$$g(t) = \frac{Y(\bar{B}c^3(t-t_0); g_0)}{c} + \frac{\bar{B}^{\frac{1}{2}}}{(c^2\bar{B} - 2K(t-t_0) + 2\Upsilon(\cos(t+\phi) - \cos(\phi+t_0)))^{\frac{1}{2}}} - \frac{1}{c}. \tag{4.9}$$

Thus the face clearance always remains positive and becomes smaller with larger gradient in region I. Figure 4.2 shows a close comparison of the full numerical solution and the asymptotic composite solution for the region, $0.7 < t < 2.9$, i.e. $t_0 = 0.7$, and parameters as listed.

The asymptotic analysis is a very simple approximation for small face clearance, used only to validate the solution of no face contact. Therefore asymptotic analysis is undertaken only in region I and II as shown in Figure 4.1. The composite solution has discrepancy with the numerical solution as the gap

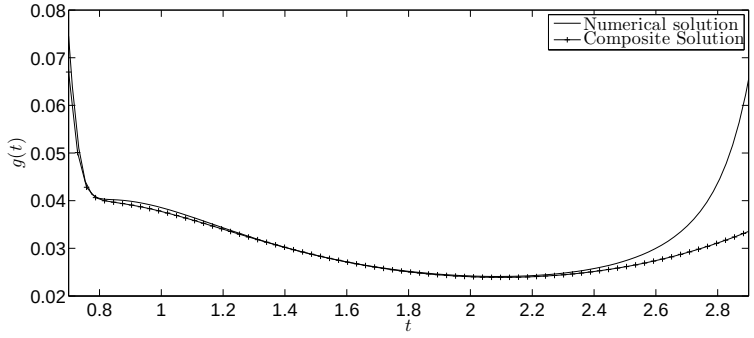

FIG. 4.2: Full numerical and composite solutions $g(t)$ for a periodic internally pressurised parallel bearing; $a = 0.8$, $\varepsilon = 1.4$, $\beta = 0$, $\lambda = 1$, $\alpha = 1$, $K_z = 10$, $\sigma = 1$, $D_a = 1$, $\bar{\sigma} = 100$, $\bar{B} = 0.0012$, $K = 10$, $\gamma = 100$, $g_0 = 0.08$ and $\phi = 0$.

grows since the asymptotics in region III were not included as they make the solution more complicated and unnecessary to show the faces do not touch.

Examining a coned bearing in the limit $g(t) \ll 1$ requires the leading order terms in the Reynolds equation for both positively and negatively coned bearings to be investigated separately. This is due to the face clearance being defined at the inner radius, $g(t)$ which is the minimum face clearance for positivity coned bearings, but negatively coned bearings have the minimum face clearance at the outer radius given by $\bar{g}(t) = g(t) - (1-a)|\beta|$. Substituting this expression into equations for $G(r)$, G_I, $H(r)$, H_I and the modified Reynolds equation will give the minimum face clearance equations for negatively coned bearings.

Since the limit is for $g(t)$ small, a restriction must be placed on the coning angle β which is also small. Thus the limit that is examined is $1 \gg g(t) \gg |\beta|$, where asymptotic analysis gives both positive and negative coning have the same behaviour in the limit, allowing the minimum face clearance in the asymptotic equation to be denoted $\hat{g}(t)$ for a coned bearing.

Equation (3.13) becomes to leading order

$$\frac{\mathrm{d}^2\hat{g}}{\mathrm{d}t^2} + \hat{B}\frac{\mathrm{d}\hat{g}}{\mathrm{d}t} + K_1\hat{g} - K_2 = \Upsilon\sin(t+\phi), \tag{4.10}$$

with positive constants $\hat{B}$, K_1 and K_2 given by

$$\begin{aligned} \hat{B} &= \alpha\pi\hat{\sigma}\frac{(1-a)}{\beta^3}, \qquad K_1 = K_z - \alpha\pi\frac{\left(p_O - p_I - \frac{\lambda}{2}(1-a^2)\right)(1-a)}{\beta\ln\left(\frac{1}{a}\right)}, \\ K_2 &= K_z + \alpha\pi\left((p_I - p_a)(1-a^2) + \frac{\lambda}{4}(1-a^2)^2\right). \end{aligned} \tag{4.11}$$

The asymptotic equation for a coned bearing in the limit $1 \gg \hat{g}(t) \gg |\beta|$ gives a second order differential equation with constant coefficients which can be solved fully. Constant $\hat{B}$ is proportional to $(\beta^3)^{-1}$ giving large damping, with equation 4.10 corresponding to a damped harmonic oscillator with sinusoidal forcing.

Equation (4.10) is solved subject to initial conditions $\hat{g}(t_0) = \hat{g}_0$ and $\mathrm{d}\hat{g}(t_0)/\mathrm{d}t = -\bar{\sigma}$ for $g(t)$ small as the numerical solution of the face clearance follows similar trend to the parallel case in region I and II as shown in Figure 4.1.

Note that a restricted limit is being sought in the coned bearing case compared to the parallel case; whilst still looking to the limit that $g(t)$ is small, the face clearance must be larger than coning, $g \gg |\beta|$. Thus the coned and parallel bearing asymptotic equations are not comparable as $\beta \to 0$.

Solving 4.10 gives the minimum face clearance as

$$\begin{aligned}\hat{g} = D\exp\left(\frac{-\hat{B}+\sqrt{\hat{B}^2-4K_1}}{2}t\right) + E\exp\left(\frac{-\hat{B}-\sqrt{\hat{B}^2-4K_1}}{2}t\right)\\ +\frac{\Upsilon}{(1-K_1)^2+\hat{B}^2}((K_1-1)\sin(t+\phi)-\hat{B}\cos(t+\phi))+\frac{K_2}{K_1},\end{aligned} \tag{4.12}$$

with constants D and E found using initial conditions $\hat{g}(0) = 1$ and $\partial\hat{g}(0)/\partial t = 0$ as

$$\begin{aligned}
D &= \frac{\exp\left(\frac{\hat{B}-\sqrt{\hat{B}^2-4K_1}}{2}t_0\right)}{\sqrt{\hat{B}^2-4K_1}}\left(-\bar{\sigma}+\left(g_0-\frac{K_2}{K_1}\right)\left(\frac{\hat{B}+\sqrt{\hat{B}^2-4K_1}}{2}\right)\right.\\
&\quad +\frac{\Upsilon}{(1-K_1)^2+\hat{B}^2}\left(\left(\hat{B}\cos(t_0+\phi)-(K_1-1)\sin(t_0+\phi)\right)\left(\frac{\hat{B}+\sqrt{\hat{B}^2-4K_1}}{2}\right)\right.\\
&\quad \left.\left.-\hat{B}\sin(t_0+\phi)-(K_1-1)\cos(t_0+\phi)\right)\right)\\
E &= \frac{\exp\left(\frac{\hat{B}+\sqrt{\hat{B}^2-4K_1}}{2}t_0\right)}{\sqrt{\hat{B}^2-4K_1}}\left(\bar{\sigma}+\left(\frac{K_2}{K_1}-g_0\right)\left(\frac{\hat{B}-\sqrt{\hat{B}^2-4K_1}}{2}\right)\right.\\
&\quad +\frac{\Upsilon}{(1-K_1)^2+\hat{B}^2}\left(\left((K_1-1)\sin(t_0+\phi)-\hat{B}\cos(t_0+\phi)\right)\left(\frac{\hat{B}-\sqrt{\hat{B}^2-4K_1}}{2}\right)\right.\\
&\quad \left.\left.+\hat{B}\sin(t_0+\phi)+(K_1-1)\cos(t_0+\phi)\right)\right)
\end{aligned} \tag{4.13}$$

Figure 4.3 shows a comparison of the full solution and asymptotic composite solution for a coned bearing in the region $0.95 < t < 2.2$. For coned bearings the analytical solution is always positive due the limit $1 \gg g(t) \gg |\beta|$, as $g(t)$ can not be smaller than $|\beta|$, giving positive face clearance. The analytical solution corroborates the numerical solutions and is therefore a useful validation of the numerical solutions.

It can be concluded that face contact does not occur for a parallel bearing or coned bearing. Since the bearing face clearance tends to zero but is finite nano-fluid effects should be considered.

5 Results

Examining different bearing parameters allows identification of potential destabilising behaviour that could lead to bearing failure at high speeds. Optimum operating conditions are identified to increase the air-film stiffness, load carrying capacity, and total damping when operating conditions are changed making it more stable. A parameter study is carried out, including changes to the coning angle, β, which

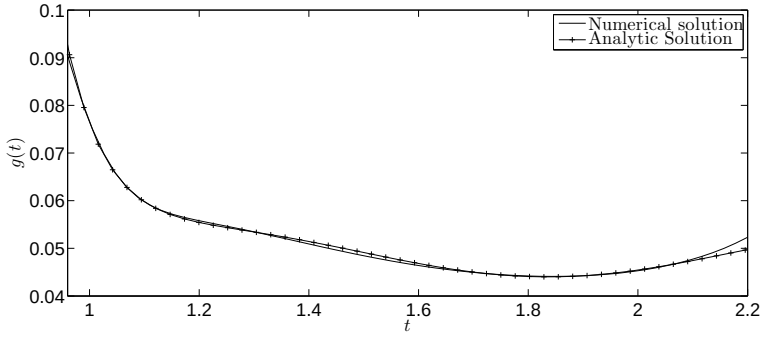

FIG. 4.3: Full numerical and composite solutions $g(t)$ for a periodic internally pressurised coned bearing; $a = 0.8$, $\varepsilon = 1.2$, $\beta = 0.001$, $\lambda = 1$, $\alpha = 1$, $K_z = 10$, $\sigma = 1$, $D_a = 1$, $\hat{B} = 100$, $K_1 = 270$, $K_2 = 13.2$, $\gamma = 1.4$, $g_0 = 0.1$, $t_0 = 0.95$, $\hat{\sigma} = 1.2$ and $\phi = 0$.

is of particular industrial interest due to the possibility of rotor distortion, to give greater understanding of interactions within the bearing. Possible destabilising behaviour at extreme operating conditions is investigated by examining the bearing when the rotor is forced with increasing oscillations. The effect of high speed operation is investigated with a study on parameter λ, modelling the effects of fluid inertia due to rotation. Structural variances are explored with a parameter study on the bearing width a, spring strength K_z, structural damping D_a and force coupling strength α.

Post-processing calculations allow the force exerted by the air-film on the stator $F(t)$ and the stator height $h_s(t)$ to be found using equations (3.9) and (3.1) respectively. Equations in (3.14) can be used to compute the fluid stiffness $K_{zf}(g)$ and total damping of the system $D(g)$. The standard bearing configuration investigated is narrow $a = 0.8$ and internally pressurised $p_O = 1, p_I = 2$ along with a negative coning angle $\beta = -0.3$ and squeeze number of $\sigma = 1$. The rotor is assumed forced with oscillations of amplitude $\varepsilon = 0.8$ with a speed parameter $\lambda = 1$. A strong spring holds the stator $K_z = 10$ and $\alpha = 1$ characterises the strength of the force coupling with damping coefficient $D_a = 1$.

The effect of decreasing bearing width on the force, stator height and face clearance are shown in Figure 5.1 over a period. The face clearance is similar to a negative sine curve becoming skewed for wide bearings. As the bearing width decreases the face clearance increases and the stator gets closer to the rotor at the minimum, with the maximum gap remaining similar. For all widths the stator oscillations have greatest magnitude when the face clearance is least. For $a \geqslant 0.6$ a local minimum force develops immediately after the maximum force, decreasing the overall per-period load carrying capacity indicating a mid-width bearing $a \approx 0.5$ has the greatest load carrying capacity. The fluid stiffness has a small magnitude except where the face clearance is small and a maximum occurs increasing with bearing width. The damping follows a broadly similar trend to the fluid stiffness.

Figure 5.2 shows the effect on the force, stator height and face clearance over one time period. The face clearance is dominated by the forced rotor oscillations and follow a path similar to a negative sine curve with the amplitude dependent upon the rotor amplitude ε. For an axially stationary rotor the bearing has constant force. Increasing the rotor oscillations causes the force to become asymmetric with large positive fluctuations in cases when the face clearance is small and negative otherwise. For large amplitude rotor oscillations, $\varepsilon > 0.7$, the force decreases rapidly below the initial value and for very

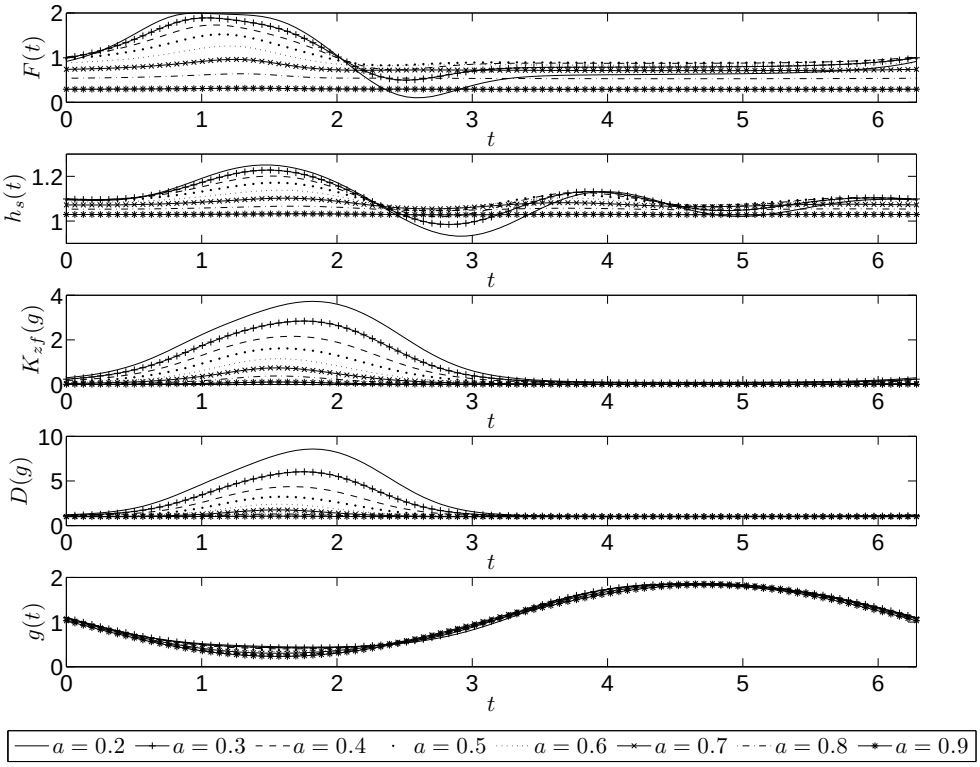

FIG. 5.1: Force, stator height, fluid stiffness, total damping and face clearance for a periodic internally pressurised bearing for decreasing radius $0.2 \leqslant a \leqslant 0.9$; $\varepsilon = 0.8$, $\beta = -0.3$, $\lambda = 1$, $\alpha = 1$, $K_z = 10$, $\sigma = 1$ and $D_a = 1$.

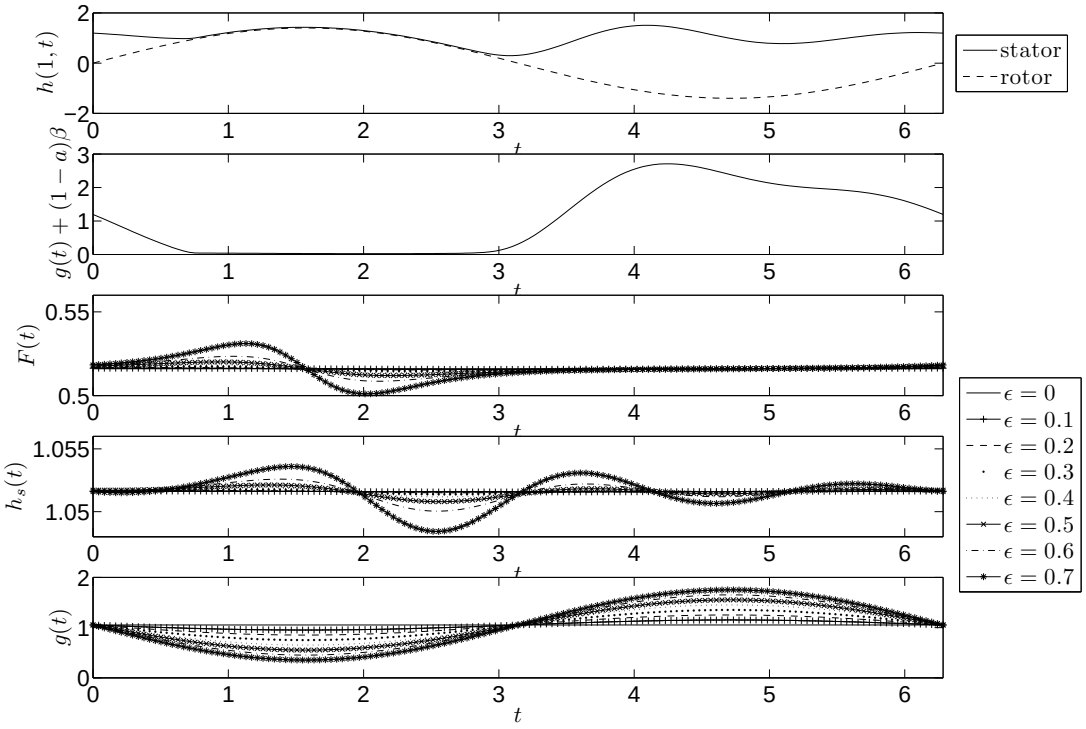

FIG. 5.2: Plots for large amplitude of oscillation $\varepsilon = 1.4$; rotor/stator position, minimum gap and plots for increasing amplitude of oscillations $0.2 \leqslant \varepsilon \leqslant 0.9$; force, stator height, face clearance for a periodic narrow internally pressurised bearing; $a = 0.8$, $\beta = -0.3$, $\lambda = 1$, $\alpha = 1$, $K_z = 10$, $\sigma = 1$ and $D_a = 1$.

large amplitudes $\varepsilon > 0.9$ a distinct minimum value is obtained. Fluid stiffness remains small and the total damping has base level $D_a = 1$ unless the face clearance is small.

Forcing the stator with amplitudes larger than the equilibrium face clearance gives interesting behaviour. Figure 5.2 shows individual stator and rotor height and face clearance over a period with amplitude $\varepsilon = 1.4$. Within a period the stator initially decreases in height until close to the rotor and then follows the path of the rotor whilst maintaining a thin air film between the two faces. The rotor pulls away from the stator just before half way through the time period. The rotor continues with its forced oscillation and the stator twice oscillates with decreasing amplitude. As the face clearance is given at the outer edge of the bearing, where it is minimum for negative coning the rotor and stator do not collide. The force, fluid stiffness and total damping follow the same trend as for $\varepsilon < 1$ but have magnitude of at least $O(10^2)$ larger. Results suggest within an incompressible model the bearing should never fail due to face contact. Numerical solutions for $\varepsilon > 1$ were obtained using the spectral solver. To maintain a quadratic rate of convergence from the solver, careful selection of the initial profile is needed. In this case the calculated solution $g(t)$ with $\varepsilon = 0.9$ was used for the initial guess for $\varepsilon = 1.0$ and successively updated.

Coning of the rotor may occur because of manufacturing imperfections/misalignment or designs to generate additional load carrying capacity; such effects are operationally important and examined. Figure 5.3 shows the periodic force on the stator, stator height and time dependent face clearance for a range of coning angles $-0.5 \leqslant \beta \leqslant 0.5$. The face clearance is similar for all coning angles with magnitude of stator fluctuations much smaller than those of the forced rotor and follow a negative sine curve. For large negative coning angles the stator oscillations are greatest when the film thickness is smallest, decaying in amplitude for the remaining time period. As the coning angle increases through positive coning angles the stator sits lower overall, with the largest change in height when the film clearance is going from its minimum to maximum value. The force on the stator is asymmetric. For a parallel face bearing the force fluctuates with equal amplitude extremum occurring when the face clearance is smallest. Increasing the coning angle $\beta > 0$ decreases the force and the minimum has larger magnitude than the maximum, whereas for negative coning angles the force increases and the maximum has larger magnitude than the minimum. The total damping has value close to the structural damping $D_a = 1$ except when the face clearance is less than its equilibrium thickness. In this case positive fluctuations occur with increasing magnitude as the coning angle goes from large positive values to large negative values. Figure 5.3 shows the fluid stiffness plotted against face clearance for increasing coning angles with the largest changes in fluid stiffness when the face clearance is smallest. There is no fluid stiffness with parallel faces and increasing/decreasing the coning angle causes the fluid stiffness to decrease/increase.

Increasing the speed parameter λ has a marked effect on the periodic force and stator height as shown in Figure 5.4 but as the stator oscillations have amplitude an order of magnitude smaller, the face clearance of the bearing is little affected. Increasing the speed parameter increases the amplitude of oscillations which are largest at small face clearances decaying over the time period. Further, the stator sits lower apart from when the face clearance is small where the order reverses for the maximum; plots cross a single point for all values of λ. When the face clearance is small the rotor causes a significant rotation within the fluid-film putting a force on the stator; the higher speed causes subsequently larger forces on the stator. However when the film clearance is large only the fluid near the rotor moves significantly and the smaller the force felt by the stator. Total damping is dominated by structural damping $D_a = 1$ apart from when the face clearance is small. The periodic fluid stiffness has very little magnitude except when the face clearance is small and there is a maximum of increasing magnitude as the speed parameter increases. Figure 5.4 shows the fluid stiffness plotted against face clearance for

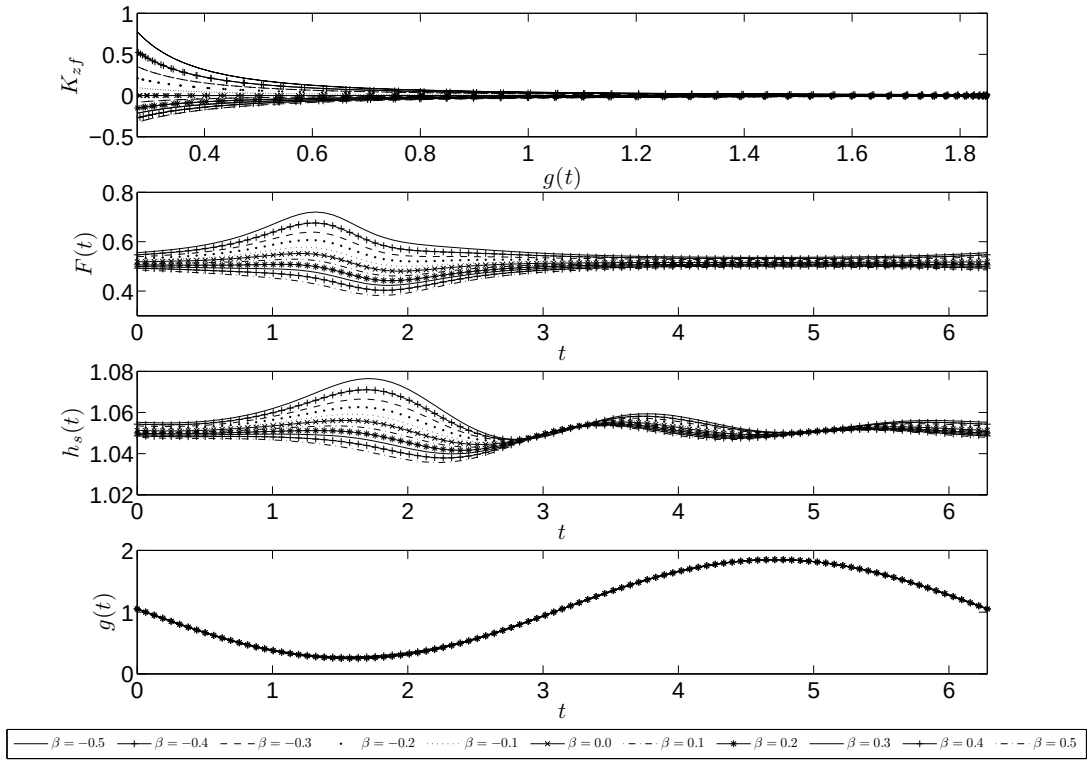

FIG. 5.3: Plots of fluid stiffness plotted against face clearance; plots of force, stator height and face clearance corresponding to a periodic narrow internally pressurised bearing for increasing coning angle $-0.5 \leqslant \beta \leqslant 0.5$; $a = 0.8$, $\varepsilon = 0.8$, $\lambda = 1$, $\alpha = 1$, $K_z = 10$, $\sigma = 1$ and $D_a = 1$

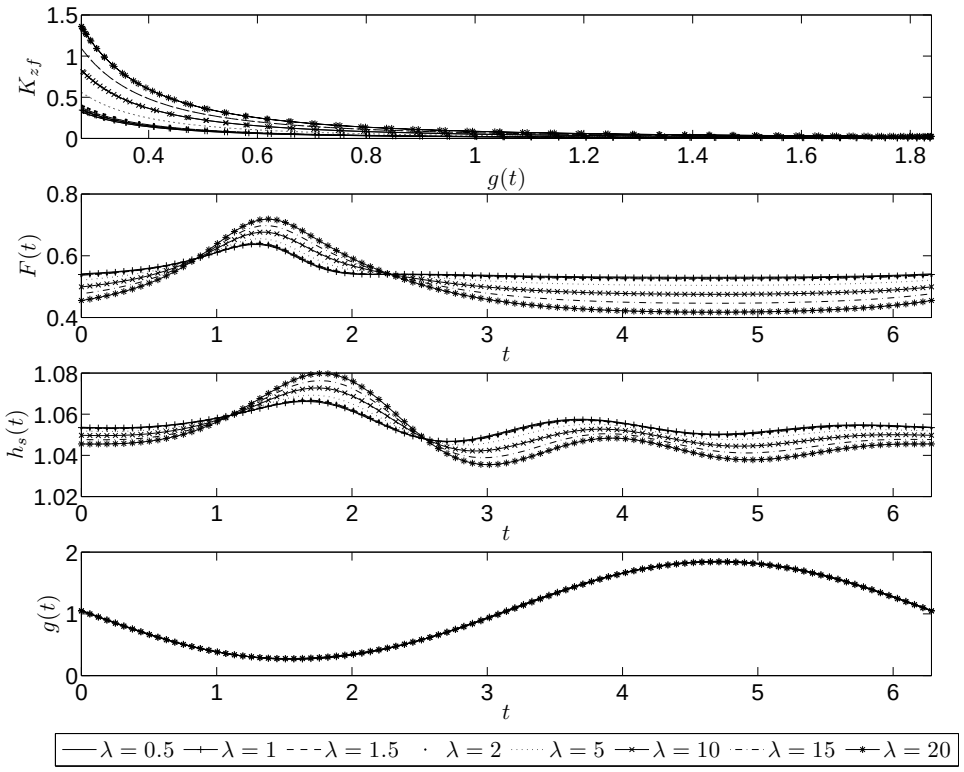

FIG. 5.4: Plots of fluid stiffness against face clearance; plots of force, stator height and face clearance corresponding to a periodic narrow internally pressurised bearing for increasing speed parameter $0.5 \leqslant \lambda \leqslant 20$; $a = 0.8$, $\varepsilon = 0.8$, $\beta = -0.3$, $\alpha = 1$, $K_z = 10$, $\sigma = 1$ and $D_a = 1$.

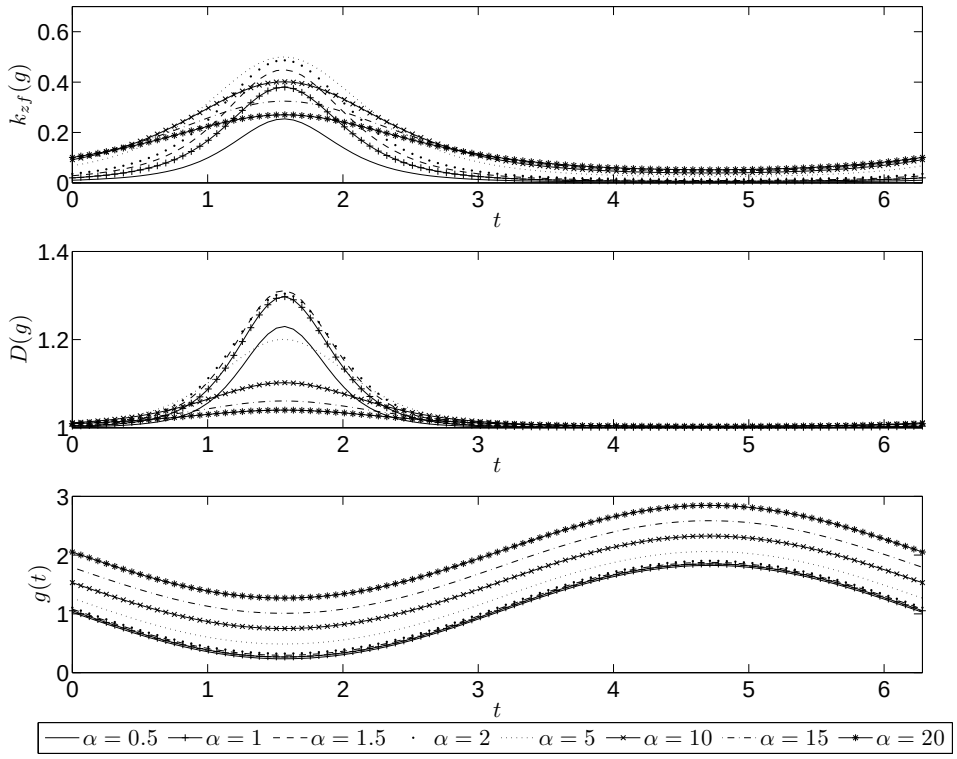

FIG. 5.5: Fluid stiffness, damping and face clearance for a periodic narrow internally pressurised bearing for increasing coupling parameter $0.5 \leqslant \alpha \leqslant 20$; $\varepsilon = 0.8$, $\beta = -0.3$, $\lambda = 1$, $\sigma = 1$, $K_z = 10$ and $D_a = 1$.

increasing speed parameter. The increase in fluid stiffness becomes more rapid as the face clearance becomes smaller and increasing the speed parameter increases the magnitude.

The parameter α quantifies the level of dynamic coupling between the bearing and flow, a range of values are used in Figure 5.5. The periodic force undergoes a small minimum when the face clearance is greater than its equilibrium height, and a maximum with increasing magnitude as the coupling parameter α decreases. The stator sits higher for larger values of α and has smaller fluctuations, though all oscillations are negligible compared to those of the forced rotor. Both the fluid stiffness and damping follow a non-linear trend not seen with other parameters. The fluid stiffness has a maximum when the face clearance is small and when the face clearance is large the fluid stiffness has a small minimum with shallow gradient. As the value of α increases the minimum increases in magnitude, however the maximum increases until $\alpha = 5$ then decrease in magnitude with shallower gradients. The total damping also takes on a similar trend when the face clearance is smaller than the equilibrium value but with the largest peak magnitude occurring when $\alpha = 1.5$, the damping is effectively constant at the structural damping $D_a = 1$ over the rest of the time period.

Investigation of the remaining parameter is discussed briefly. Different bearing pressurisations are

analysed in periodic plots, with external and internal pressurised bearings having similar face clearance, with asymmetric force and stator height. Bearings with no imposed pressure gradient have face clearance and stator height of smaller magnitude and negative force indicating no load carrying capacity. The total damping has a maximum when the face clearance is small, with largest magnitude when no pressure gradient is imposed on the bearing. The fluid stiffness is zero for no imposed pressure gradient and maximum when there is a diverging channel in the direction of pressure gradient and minimum with a converging channel. The structural stiffness parameter represents flexible attachment of the stator to its housing unit and can be tuned to modify the dynamics of the bearing; increasing the spring constant increases the height of the stator. The stator sits closer to the rotor for increasing spring strength thus reducing the face clearance and increasing the force when the face clearance is small. The fluid stiffness and total damping both have a maximum when the face clearance is small with increasing magnitude as the spring parameter increases. Increasing the squeeze number, which models the effect of rotor forcing frequency causes, increases in fluctuations of stator height and force when the face clearance is small. The face clearance has a slight difference at the extremum but still follows a negative sine curve. The fluid stiffness maximum decreases with increasing squeeze number whereas the total damping increases. Increasing the damping coefficient has little effect on the force fluctuations, minimum face clearance and fluid stiffness. The stator oscillations decrease with increasing the damping coefficients as does the total damping.

6 Summary and Conclusion

A modified Reynolds equation for incompressible flow is derived for a bearing containing a rigid coned rotor using an axisymmetric lubrication approximation but retaining the leading order effect of centrifugal inertia relevant for high speed flows. The derivation includes detailed consideration of the velocity boundary conditions needed to include the coned rotor surface. The stator equation is derived as a spring-mass-damper system.

Investigating the air-rotor-stator interaction, the fully coupled unsteady bearing is examined where the stator motion is coupled to the film dynamics via the axial force exerted on the stator by the air-film. Re-writing the modified Reynolds equation and the stator equation in terms of a new variable, the time dependent face clearance $g(t)$, allows explicit analytic expressions for the pressure, force and a nonlinear second-order non-autonomous ordinary differential modified stator equation to be derived. Motivation for seeking a solver for periodic solutions comes from the numerical solutions to the modified stator equation. The solutions are found via a transient solver and achieve stable periodic solutions. A spectral collocation numerical scheme is implemented and post-processing allows computation of the force on the stator, stator height, fluid stiffness and damping. Analysis of an initial transient shows that within a small gap asymptotic study shows no rotor/stator contact is made.

In the absence of an imposed pressure gradient it is shown that negative force occurs reducing the load carrying capacity. Extensive results and investigation is provided for pressurised bearing cases. Inner and outer pressurisations are not too dissimilar, resulting in either being suitable for practical operation. Results show the narrower the bearing the more stable it becomes with the stator sitting closer to the rotor and the fluid stiffness and total damping have a smaller fluctuation when the face clearance is small, but the load carrying capacity is reduced. Investigating possible destabilising behaviour for extreme operating conditions is simulated by forced rotor oscillations, showing that for $\varepsilon \leqslant 0.8$ the load carrying capacity of the bearing is similar but for larger amplitudes it has a reduced load carrying capacity. The stator becomes more unstable as the rotor oscillations increase, becoming displaced and following the rotor when $\varepsilon > 1$ but maintaining a small air-film between the two elements. However, in

practice face contact would most likely occur as the air-film is so thin at this point. Increasing the amplitude of rotor oscillation, causes the fluctuation in fluid stiffness and total damping to have increased magnitude from their effectively constant values of very small magnitude and structure damping $D_a = 1$, respectively. Larger negative values of coning angles β increase the force and thus the load carrying capacity as well as the fluid stiffness and total damping, but this also increases the stator oscillations, making the bearing more unstable. Therefore an optimum coning angle is a comprise between the load carrying capacity and stability of the bearing. Decreasing the speed parameter decreases the oscillations in stator height and axial force increasing the stability and load carrying capacity but gives higher damping and lower fluid stiffness. Smaller values of coupling parameter α causes the stator to sit closer to rotor and have larger total damping. The axial force has the greatest overall magnitude when α takes a mid-small value giving the greatest load carrying capacity and the stiffness has a greater average for larger values of α. The larger the stiffness parameter the greater the fluid stiffness and total damping in the bearing, with the stator sitting closer to the rotor, although for $K_z \geqslant 10$ there is not much height difference. The average force per cycle is greatest for $5 \leqslant K_z \leqslant 10$, implying this is when the bearing has the greatest load carrying capacity. The natural frequency of the system is given by $\sqrt{K_z}$ giving the natural frequency as 1 and no natural resonance is identified owing to the damping in the system. A low squeeze number increases the load carrying capacity as it decreases the force fluctuations and stator oscillations reduce. The total damping and fluid stiffness fluctuation decreases when the face clearance is small. The damping coefficient has little effect on the force and fluid stiffness, but increasing the damping coefficient causes the stator to sit lower with the base value for the damping taking the value $D_a = 1$.

Acknowledgement

The authors wish to acknowledge the contribution of Dr. J. E. Garratt, Rolls Royce plc, Aerospace Group, in providing motivation and support for this study.

References

AGRAWAL, G. (1997) Foil air/gas bearing technology - an overview, *ASME,* Publication 97-GT-347.

BATCHELOR, G.K. (1967) *An introduction to fluid dynamics,* Cambridge University Press.

BRUNETIÉRE, N. & TOURNERIE, B. (2006) The effect of inertia on radial flows - application to hydrostatic seals, *ASME Journal of Tribology,* **128**, 566–574.

BRUNETIÉRE, N., TOURNERIE, B. & FRÊNE, J. (2003) TEHD lubrication of mechanical face seals in stable tracking mode: Part 1: - numerical model and experiments, *ASME Journal of Tribology,* **125**, 608–616.

BRUNETIÉRE, N., TOURNERIE, B. & FRÊNE, J. (2003) TEHD lubrication of mechanical face seals in stable tracking mode: Part 2: - parametric study, *ASME Journal of Tribology,* **125**,617–627.

ETISON, I. (1982) Dynamic analysis of noncontacting face seals, *Transactions of the ASME,* **104**, 460–468.

GARRATT, J.E., CLIFFE, K.A, HIBBERD, S. & POWER, H. (2010) A compressible flow model for the air-rotor-stator dynamics of a high-speed squeeze-film thrust bearing, *Journal of Fluid Mechancics,* **655**, 446–471.

GARRATT, J.E., CLIFFE, K.A, HIBBERD, S. & POWER, H. (2012) Centrifugal inertia effects in high speed hydrostatic air thrust bearings, *Journal of Engineering Mathematics, Journal of Engineering Mathematics,* DOI: 10.1007/s10665-011-9527-8

GREEN, I. (1987) The rotor dynamic coefficients of coned-face mechanical seals with Inward or Outward Flow, *Journal of Tribology,* **109**, 129–135.

GREEN, I. & ETISON, I. (1983) Fluid film dynamic coefficients in mechanical face seals, *Journal of Lubrication Technology,* **105**, 297–302.

HASEGAWA, E. & IZUCHI, H. (1982) Inertia effects due to lubricant compressibility in a sliding externally pressurized gas bearing, *Wear,* **80**, 207–220.

ITOH, M., YAMADA, Y., IMAO, S. & GONDA, M. (1991) Experiments on turbulent flow due to an enclosed rotating disk, *Experimental Thermal and Fluid Science,* **5**(3), 359–368.

LYGREN, M. & ANDERSSON, H.I. (2000) Turbulent flow between a rotating and a stationary disk, *Journal of fluid mechanics,* **426**, 297–326.

MCDARBY, J.M. & SMITH, F.T. (2007) Turbulent flow on a planar moving belt and a rotating disk: modelling and comparisons, *Journal of fluid mechanics,* **587**, 255–270.

MALANOSKI, S. & WALDRON, W. (1973) Experimental investigation of air bearings for gas turbine engines, *ASLE Transactions,* **16**, 297–303.

MALVANO, R., VATTA F., & VIGLIANI, A. (1999) Lubricated Plane Slider Bearing: Analytic and Numerical Approach, *Meccanica,* **34**(4) , 237–250.

PARKINS, D.W. & STANLEY, W.T. (1982) Characteristics of an oil squeeze film, *Journal of Lubrication Technology,* **104**, 497–502.

SALBU, E. (1964) Compressible squeeze films and squeeze bearings, *Transaction of the ASME Journal of Basic Engineering,* **86**, 355–366.

SAN ANDRÉS, L. & CHIRATHADAM, T.A. (2011) Identification of rotordynamic force coefficients of a metal mesh foil bearing using impact load excitations, *Journal of Engineering for Gas and Turbines Power,* **133**(11), 112501 1-9.

SAN ANDRÉS, L. & KIM, T.H. (2008) Analysis of gas foil bearings integrating FE top foil models, *Tribology International,* **42**(1),111-120.

SAYMA, A.I., BRÉARD, C., VAHDATI M. & IMREGUN M. (2002) Aeroelasticity analysis of air-riding seals for aero-engine applications, *Journal of Tribology,* **124**(3), 607–616.

SMITH, F.T., LI, L. & WU, G.X. (2003) Air cushioning with a lubrication/inviscid balance, *Journal of fluid mechanics,* **482**, 291–318.

TREFETHEN, L.N. (2000) *Spectral Methods in MATLAB,* SIAM, Philadelphia.

TUCK, E.O. & BENTWICH, M. (1983) Sliding sheets: lubrication with comparable viscous and inertia forces *Journal of fluid mechanics,* **135**(3), 51–69.

ZIRKELBACK, E.& SAN ANDRÉS, L. (1999) Effect of frequency excitation on force coefficients of spiral groove gas seals, *Journal of Tribology,* **121**(4), 853–863.

WILSON, S.K.& DUFFY, B.R. (1998) On lubrication with comparable viscous and inertia forces, *The Quarterly Journal of Mechanics and Applied Mathematics ,* **51**(1), 105–124.

WITELSKI, T.P. (1998) Dynamics of air bearing sliders, *Physics of fluids,* **10**(3), 698–708.

WITELSKI, T.P. & HENDRIKS, F. (2008) Stability of Gas Bearing Sliders for Large Bearing Number: Convective Instability of the Tapered Slider, *Tribology Transactions,* **42**(1), 216–222.

WOLFRAM MATHWORLD (2011) Newton-Raphson method, accessed January 2012, *http://mathworld.wolfram.com/NewtonsMethod.html*

APPENDIX

A Derivation of Reynolds Equation

A model for the incompressible air-flow through the bearing may be derived from the Navier-Stokes momentum and continuity equations

$$\hat{\rho}\left(\frac{\partial \hat{\mathbf{u}}}{\partial \hat{t}} + (\hat{\mathbf{u}}\cdot\hat{\nabla})\hat{\mathbf{u}}\right) = -\hat{\nabla}\hat{p} + \mu\hat{\nabla}^2\hat{\mathbf{u}} + \mathbf{b}, \qquad \hat{\nabla}\cdot\ \hat{\mathbf{u}} = 0, \tag{A.1}$$

where ρ is the density, μ the dynamic viscosity and $\mathbf{b}$ represents external body forces such as gravity.

It is assumed that the bearing configuration is axisymmetric and the velocity field is $\widehat{\mathbf{u}} = (\widehat{u}, \widehat{v}, \widehat{w})$ in cylindrical polar co-ordinates. Thus the radial, azimuthal and axial components of the axially symmetric Navier-Stokes momentum and continuity equations for incompressible flow (A.1) are

$$\rho\left(\frac{\partial \hat{u}}{\partial \hat{t}} + \hat{u}\frac{\partial \hat{u}}{\partial \hat{r}} + \hat{w}\frac{\partial \hat{u}}{\partial \hat{z}} - \frac{\hat{v}^2}{\hat{r}}\right) = -\frac{\partial \hat{p}}{\partial \hat{r}} + \mu\left(\hat{\nabla}^2\hat{u} - \frac{\hat{u}}{\hat{r}^2}\right), \tag{A.2a}$$

$$\rho\left(\frac{\partial \hat{v}}{\partial \hat{t}} + \hat{u}\frac{\partial \hat{v}}{\partial \hat{r}} + \hat{w}\frac{\partial \hat{u}}{\partial \hat{z}} + \frac{\hat{u}\hat{v}}{\hat{r}}\right) = \mu\left(\hat{\nabla}^2\hat{v} - \frac{\hat{v}}{\hat{r}^2}\right), \tag{A.2b}$$

$$\rho\left(\frac{\partial \hat{w}}{\partial \hat{t}} + \hat{u}\frac{\partial \hat{w}}{\partial \hat{r}} + \hat{w}\frac{\partial \hat{w}}{\partial \hat{z}}\right) = -\frac{\partial \hat{p}}{\partial \hat{z}} + \mu\left(\hat{\nabla}^2\hat{w}\right) - \hat{\rho}g, \tag{A.2c}$$

$$\frac{1}{\hat{r}}\frac{\partial}{\partial \hat{r}}(\hat{r}\hat{u}) + \frac{\partial \hat{w}}{\partial \hat{z}} = 0, \tag{A.2d}$$

in cylindrical polar coordinates.

Applying the non dimensional scalings in section 2 the Navier-Stokes momentum and continuity

equations the the radial, azimuthal and axial components (A.1a)-(A.1c) become respectively

$$Re_U\delta_0^2\left(\sigma\frac{\partial u}{\partial t}+u\frac{\partial u}{\partial r}+\sigma w\frac{\partial u}{\partial z}-(Re^*)^2\frac{v^2}{r}\right) = -\frac{Ph_0^2}{\mu r_R U}\frac{\partial p}{\partial r}+\frac{\partial^2 u}{\partial z^2} + \delta_0^2\left(\frac{1}{r}\frac{\partial}{\partial r}\left(r\frac{\partial u}{\partial r}\right)-\frac{u}{r^2}\right), \quad \text{(A.3a)}$$

$$Re_U\delta_0^2\left(\sigma\frac{\partial v}{\partial t}+u\frac{\partial v}{\partial r}+\sigma w\frac{\partial v}{\partial z}+\frac{uv}{r}\right) = \frac{\partial^2 v}{\partial z^2}+\delta_0^2\left(\frac{1}{r}\frac{\partial}{\partial r}\left(r\frac{\partial v}{\partial r}\right)-\frac{v}{r^2}\right), \quad \text{(A.3b)}$$

$$Re_U\sigma\delta_0^4\left(\sigma\frac{\partial w}{\partial t}+u\frac{\partial w}{\partial r}+\sigma w\frac{\partial w}{\partial z}\right) = -\frac{Ph_0^2}{\mu r_R U}\frac{\partial p}{\partial z}+\sigma\delta_0^2\frac{\partial^2 w}{\partial z^2} + \sigma\delta_0^4\frac{1}{r}\frac{\partial}{\partial r}\left(r\frac{\partial w}{\partial r}\right)-\frac{Re_U\delta_0^3}{Fr^2}, \quad \text{(A.3c)}$$

and the continuity equation (A.2d) becomes

$$\frac{1}{r}\frac{\partial}{\partial r}(ru)+\sigma\frac{\partial w}{\partial z}=0. \quad \text{(A.4)}$$

Definitions of the radial and azimuthal Reynolds numbers, Re_U and Re_Ω, respectively, along with the Reynolds number ratio Re^* are given in (2.8) and the aspect ratio δ_0, squeeze number σ and Froude number Fr are shown in (2.9).

The aspect ratio is very small, $\delta_0 \ll 1$ justifying the use of a lubrication approximation. Classical lubrication theory allows all inertia to be neglected due to the reduced Reynolds number being small, $Re_U\delta_0^2 \ll 1$. However, in the case of high-speed bearing operation the ratio of the Reynolds numbers Re^* is not always negligible.

Applying the above conditions and assumptions to the momentum equations (A.3) gives leading order equations

$$-\eta\frac{v^2}{r} = -\frac{\partial p}{\partial r}+\frac{\partial^2 u}{\partial z^2}, \quad \text{(A.5a)}$$

$$0 = \frac{\partial^2 v}{\partial z^2}, \quad \text{(A.5b)}$$

$$0 = \frac{\partial p}{\partial z}, \quad \text{(A.5c)}$$

where the speed parameter $\eta = Re_U\delta_0^2(Re^*)^2 = \rho r_0 h_0^2\Omega^2/\mu U$ models the effect of inertia due to rotation.

Similarly the continuity equation (A.4) becomes

$$\frac{1}{r}\frac{\partial}{\partial r}(ru)+\sigma\frac{\partial w}{\partial z}=0. \quad \text{(A.6)}$$